Supplementary Data

This supplementary data is a part of a paper entitled "Influence of Hydrothermal Parameters on Photocatalytic Activity of $BiVO_4$ for Degradation of Methylene Blue".

Crystal Structure

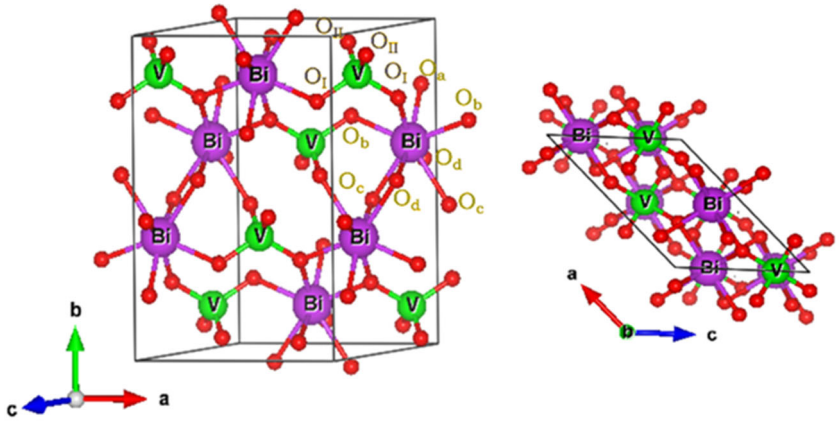

Fig S1. Unit cell structure obtained from refinement and visualized by Vesta software

Analysis of XRD diffraction peak broadening

The Williamson-Hall method is a popular tool for analyzing the peak broadening phenomenon observed in X-ray diffraction (XRD) patterns. It attributes the peak broadening to the synergistic effect of domain size and strain-induced distortion [1]. This method is encapsulated in the following expression:

$$\beta^* = \frac{1}{D} + 2\varepsilon d^* \quad (1)$$

where, D symbolizes the volume-weighted domain size and ε represents the upper limit or maximum strain within the lattice. The simplified integral breadth, denoted as β^*, is a product of peak breadth (β), diffraction angle (θ), and X-ray wavelength (λ), expressed as $\beta\cos(\theta)\lambda^{-1}$. Similarly, d^* is defined as $2\sin(\theta)\lambda^{-1}$. Eq. (1), more commonly preferred to as the Uniform Deformation Model (UDM), presumes isotropic strain distribution. The plot of β^* against d^* provides the information of uniform lattice strain, quantifiable through the slope, and the average domain size, determinable from the y-intercept. However, the homogeneous or isotropic strain is not completely true for real crystals. Therefore, modified versions of Williamson-Hall method have been introduced to better respond to realistic conditions, including the Uniform Stress Deformation Model (USDM) and the Uniform Deformation Energy Density Model (UDEDM) [2]. The USDM is represented as follows.

$$\beta^* = \frac{1}{D} + 2\sigma\frac{d^*}{E(hkl)} \quad (2)$$

USDM, described by Eq. (2), considers anisotropic strain while it assumes that crystals experience uniform stress. In this model, the uniform stress σ is defined as the product of strain ε and Young's modulus E(hkl) specific to the crystallographic plane (hkl). For monoclinic structures, the stationary value of Young's modulus, E(hkl), can be approximated through Eq. (3) [3];

$$\frac{1}{E(hkl)} = \frac{1}{3}\left[\gamma_1 + \gamma_2 + \gamma_3 + (S_{11} - \gamma_1)n_1^2 + (S_{22} - \gamma_2)n_2^2 + (S_{33} - \gamma_3)n_3^2\right] \quad (3)$$

where γ_i is calculated by Eq. (4-6), S_{ij} is the elastic compliance given in Table S1, and n_i are direction cosines determined as Eq. (7).

$$2\gamma_1 = S_{44} + 2S_{23} \quad (4)$$

$$2\gamma_2 = S_{55} + 2S_{13} \quad (5)$$

$$2\gamma_3 = S_{66} + 2S_{12} \quad (6)$$

$$n_1^2 = \frac{h^2}{1/d_{hkl}^2}; n_2^2 = \frac{k^2}{1/d_{hkl}^2}; n_3^2 = \frac{l^2}{1/d_{hkl}^2} \quad (7)$$

Table S1. The elastic compliance matrix S_{ij} of monoclinic $BiVO_4$ ($S_{ij}=C_{ij}^{-1}$, in which C_{ij} is retrieved from a previous study [4])

S_{ij}	S_{i1}	S_{i2}	S_{i3}	S_{i4}	S_{i5}	S_{i6}
S_{1j}	0.01471	0.00022	−0.0062	0	0.00694	0
S_{2j}	0.00022	0.01083	−0.00369	0	0.00153	0
S_{3j}	−0.0062	−0.00369	0.01002	0	−0.00476	0
S_{4j}	0	0	0	0.02548	0	−0.00098
S_{5j}	0.00694	0.00153	−0.00476	0	0.02043	0
S_{6j}	0	0	0	−0.00098	0	0.02751

The uniform stress in the USDM is determined from the slope of the plot of β^* against $d^*\times E(hkl)^{-1}$ and, consequently, lattice strain. Regarding UDEDM, the assumption of this model is that the deformation energy $u = 0.5\varepsilon^2 E(hkl)$ is uniform across all crystal orientations. Therefore, the Eq. (1) is modified as below.

$$\beta^* = \frac{1}{D} \pm 2\sqrt{2u}\left(\frac{d^*}{\sqrt{E(hkl)}}\right) \quad (8)$$

The lattice strain can be identified via the energy density u, which is the slope of the plot of β^* against $d^*\times E(hkl)^{-0.5}$. However, it is important to note that the implicit assumption of Williamson-Hall methods is that line profiles are Lorentzian, which is unlikely to occur in practice. Instead, Halder-Wagner [5] proposed the integral breadth of line profiles is Voigtian and is represented as:

$$\beta^{*2} = \beta_L\beta + {\beta_G}^2 \quad (9)$$

in which the Lorentzian component (β_L) and Gaussian component (β_G) are due solely to size effect ($\beta_L=D^{-1}$) and strain ($\beta_G= 0.5\eta d^*$, where $\eta\approx 5\varepsilon$), respectively. Therefore, Eq. (9) can be rewritten as below.

$$\left(\frac{\beta^*}{d^*}\right)^2 = \frac{1}{D}\left(\frac{\beta^*}{d^{*2}}\right) + \left(\frac{\eta}{2}\right)^2 \quad (10)$$

The slope and the intercept of the linear model provide information about the domain size and the lattice strain, respectively.

Table S2. Parameters of linear models used in the analysis of XRD peak broadening

Method	Temperature (°C)	Slope	Intercept	Adj.R-squared
UDM	150	-2.29×10^{-4}	1.49×10^{-3}	0.144
	200	-7.17×10^{-4}	2.12×10^{-3}	0.600
	220	5.20×10^{-4}	2.81×10^{-3}	0.058
USDM	150	-1.87×10^{-4}	1.40×10^{-3}	−0.019
	200	-2.73×10^{-4}	1.80×10^{-3}	0.025
	220	-1.10×10^{-3}	3.10×10^{-3}	0.054

Method	Temperature (°C)	Slope	Intercept	Adj.R-squared
UDEDM	150	-1.72×10^{-4}	1.40×10^{-3}	0.010
	200	-4.86×10^{-4}	1.90×10^{-3}	0.110
	220	-5.40×10^{-4}	3.10×10^{-3}	0.015
Halder-Wagner	150	1.56×10^{-3}	-1.3×10^{-6}	0.998
	200	2.12×10^{-3}	-3.10×10^{-6}	0.998
	220	3.23×10^{-3}	-3.85×10^{-6}	0.996
	pH 1.0	1.82×10^{-3}	-2.01×10^{-6}	0.999

Optical Properties

Bandgap energy is typically determined by Tauc plot extrapolation, which includes finding the intersection between the linear model of absorption threshold and the photon energy axis. The following analysis estimates indirect band gap energy of $BiVO_4$ using Tauc method with three distinct fitting ranges. Although these linear models have high R^2 values, the fluctuation of the obtained band gap energies suggests that the errors could arise during calculation by operators.

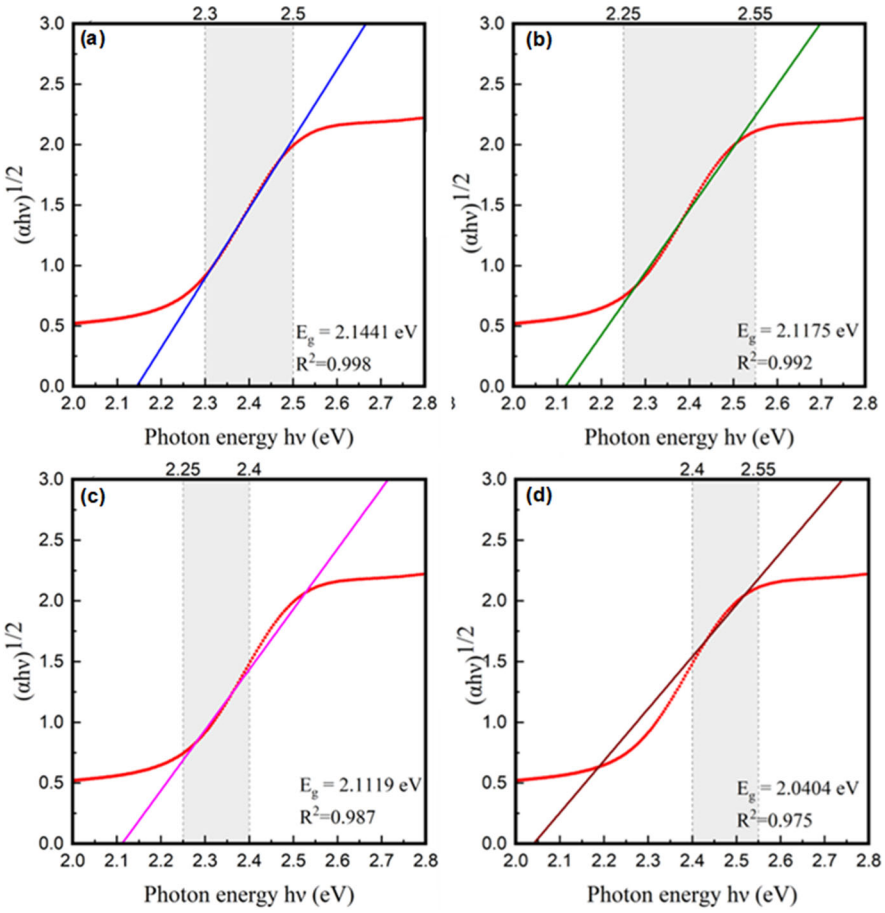

Fig S2. The indirect bandgap energies are determined by linear regression with different fitting ranges

Photocatalytic Activity

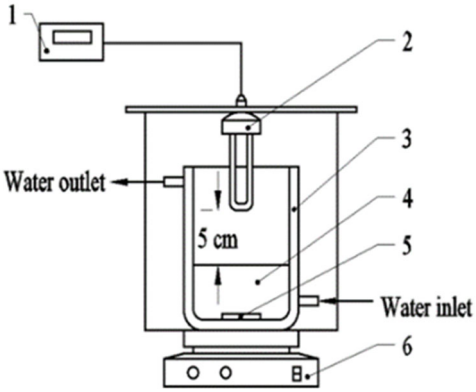

Fig S3. Schematic of experimental apparatus of photocatalysis and spectrum of the light source. (1) Power supply; (2) Simulated sunlight lamp; (3) Jacketed glass beaker; (4) Tested solution; (5) Magnetic bar; (6) Magnetic stirrer

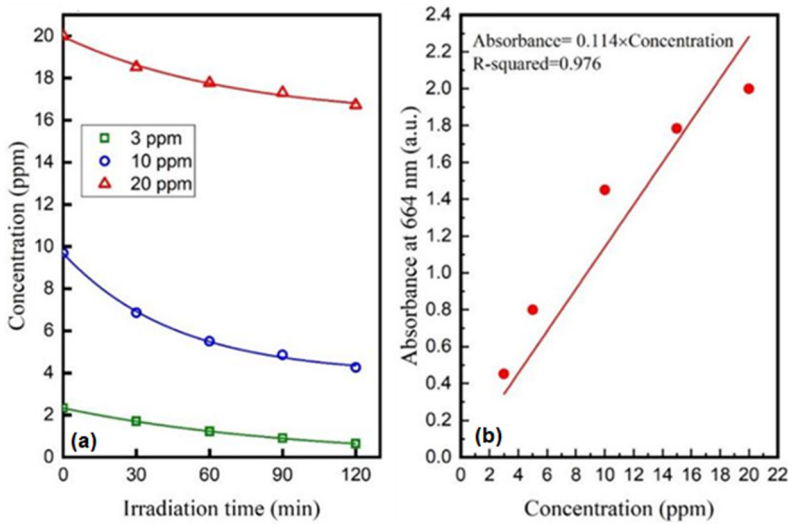

Fig S4. (a) Degradation plots of MB solution with different initial concentrations using the sample prepared at 200 °C, pH 0.5, 10 h; (b) Linear correlation between the absorbance and the concentration of MB

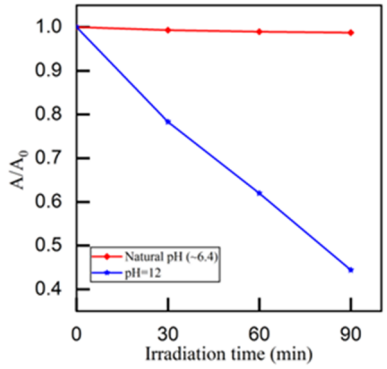

Fig S5. Self-decomposition of methylene blue under irradiation in the absence of photocatalyst

Table S3. First-order kinetic rate constants of the degradation of MB using samples prepared at various hydrothermal conditions

Temperature (°C)	Time (h)	pH	k.10² (min⁻¹)	R²
150	10	0.50	0.689	0.97
200	10	0.50	0.762	0.98
220	10	0.50	0.358	0.99
200	6	0.50	0.628	0.98
200	10	0.50	0.762	0.97
200	24	0.50	0.700	0.96
200	10	0.25	0.648	0.98
200	10	0.50	0.762	0.99
200	10	0.75	0.799	0.97
200	10	1.00	1.015	0.97
200	10	1.50	0.934	0.97
200	10	2.00	0.758	0.96
200	10	2.50	0.724	0.96
200	10	3.00	0.779	0.96

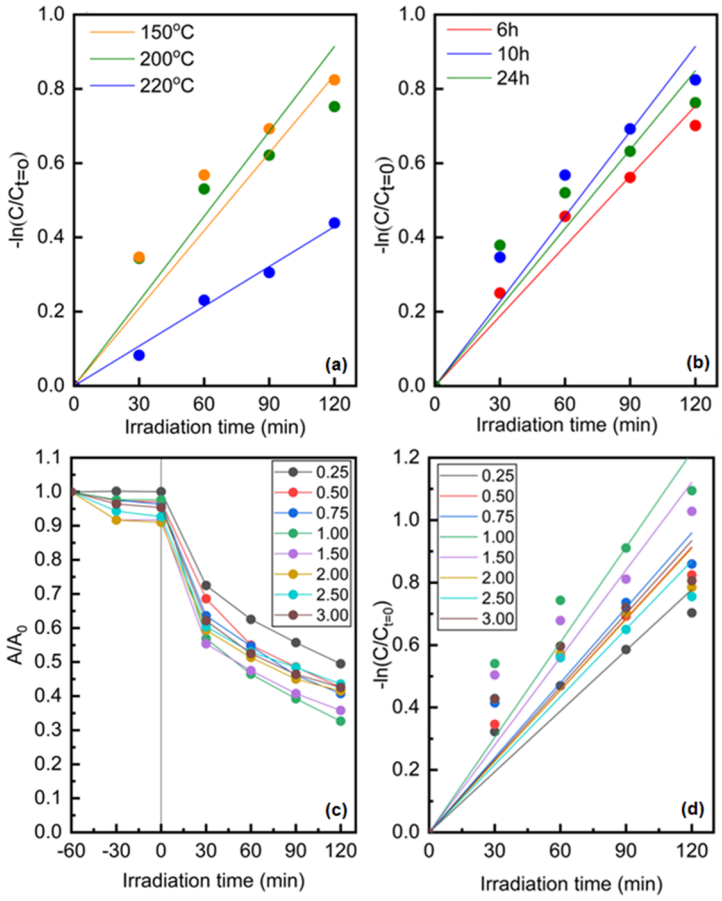

Fig S6. First-order kinetic curve for the degradation of MB using samples synthesized at different (a) hydrothermal temperature, (b) hydrothermal duration, (c) decay profiles for the degradation of MB using samples prepared at various pH levels, (d) pH levels

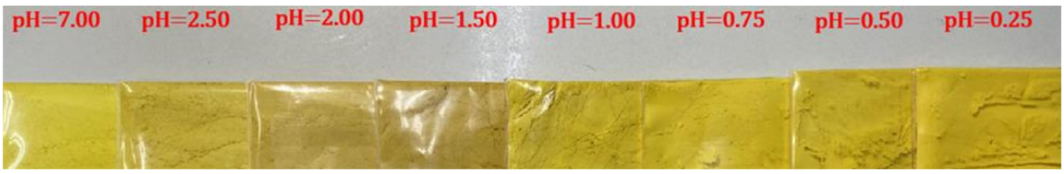

Fig S7. Color dependence of BiVO4 powder fabricated at various pH levels

Table S4. Comparison in photocatalytic activity of recent $BiVO_4$-based catalysts and other catalysts in the degradation of MB

Photocatalyst	Synthesis method of $BiVO_4$	Light source	C_0	Kinetic rate constant (k)	Ref.
(HEC-PVA)/(Cu_2O@rGO)/$BiVO_4$	Hydrothermal	100W lamp	10 ppm	1.270×10^{-2} min^{-1} (at pH=11)	[6]
$BiVO_4$-GO-PVDF	Hydrothermal + Ultrasonic	500W lamp	20 ppm	5.300×10^{-3} min^{-1}	[7]
$BiVO_4$-paint	Calcination	2×15W Havells bulbs	5 ppm	0.524×10^{-2} min^{-1}	[8]
Titanate-$BiVO_4$ thin film	Electrophoretic deposition, chemical solution growth	Xenon lamp (100mW/cm^2)	50 µM	0.500×10^{-2} min^{-1}	[9]
$BiVO_4$/$BaSnO_3$@HNT	Hydrothermal	200W LED lamp	20 ppm	1.15567 h^{-1}	[10]
$BiVO_4$ (truncated square hexagonal bipyramid)	Solvothermal	1000W Xenon lamp (λ>420 nm)	20 ppm	0.380×10^{-2} min^{-1}	[11]
$BiVO_4$ (leaf-like shape)	Solvothermal	6 daylight LED 10W	15 ppm	0.770×10^{-2} min^{-1}	[12]
rGO/$BiVO_4$	Co-precipitation + hydrothermal	54W Essential MO, Philips	3 ppm	0.670×10^{-2} min^{-1} (pristine $BiVO_4$) 1.440×10^{-2} min^{-1} (rGO/$BiVO_4$)	[13]
$BiVO_4$ doped 6% Yb^{3+}, 3% Er^{3+}, 3% Tm^{3+}	Microwave hydrothermal	100W NIR lamp	20 ppm	0.276×10^{-2} min^{-1}	[14]
$ZnFe_2O_4$/$BiVO_4$	Co-precipitation	500W halogen lamp	10 ppm	0.370×10^{-2} min^{-1} (pristine $BiVO_4$) 1.320×10^{-2} min^{-1} ($ZnFe_2O_4$/$BiVO_4$)	[15]
$Bi_2VO_{5.5}$	Mechanochemical ball milling	2×15W Havells bulbs	5 ppm	0.636×10^{-2} min^{-1}	[16]
$BaSn_{0.99}W_{0.01}O_3$	Co-precipitation	200W LED panel	5 ppm	0.560×10^{-2} min^{-1}	[17]
ZnO/activated carbon	_	UV lamp	5 ppm	3.490×10^{-3} min^{-1}	[18]
$BiVO_4$	Hydrothermal	26W simulated sunlight	10ppm	1.015×10^{-2} min^{-1}	This work

Reference

[1] Balzar, D., and Popović, S., 1996, Reliability of the simplified integral-breadth methods in diffraction line-broadening analysis, *J. Appl. Crystallogr.*, 29 (1), 16–23.

[2] Patel, K., Patel, A., Jethwa, V.P., Patel, H., and Solanki, G.K., 2024, X-ray diffraction analysis of orthorhombic SnSe nanoparticles by Williamson–Hall, Halder–Wagner and Size–Strain plot methods, *Chem. Phys. Impact*, 8, 100547.

[3] Ting, T.C.T., 2005, The stationary values of young's modulus for monoclinic and triclinic materials, *J. Mech.*, 21 (4), 249–253.

[4] Fisher, E.S., 1989, Elastic moduli and acoustic symmetry of ferroelastic $LaNbO_4$ and $BiVO_4$, *J. Phys.: Condens. Matter*, 1 (17), 2875.

[5] Halder, N.C., and Wagner, C.N.J., 1966, Separation of particle size and lattice strain in integral breadth measurements, *Acta Crystallogr.*, 20 (2), 312–313.
[6] Mohamed, A.M., Abdelwahab, S.M., Elsawy, N.M., Ahmed, N.A., and Raafat, A.I., 2024, E-beam irradiation-induced synthesis of hydroxyethyl cellulose/(Cu_2O-rGO)/$BiVO_4$-based nanocomposite for photocatalytic remediation of wastewater under visible light, *Int. J. Biol. Macromol.*, 258, 128681.
[7] Biswas, M.R.U.D., and Oh, W.C., 2018, Synthesis of $BiVO_4$-GO-PVDF nanocomposite: An excellent, newly designed material for high photocatalytic activity towards organic dye degradation by tuning band gap energies, *Solid State Sci.*, 80, 22–30.
[8] Kumar, M., and Vaish, R., 2022, Photocatalytic dye degradation using $BiVO_4$–paint composite coatings, *Mater. Adv.*, 3 (14), 5796–5806.
[9] Kulkarni, S.P., Chitare, Y.M., Magdum, V.V, Sawant, P.D., Talekar, S.V., Pawar, S.A., Malavekar, D.B., Ansar, S., Kim, J.H., and Gunjakar, J.L., 2024, Nanohybrids of layered titanate and bismuth vanadate as visible-light-driven photocatalysts for the degradation of dyes and antibiotic, *ACS Appl. Nano Mater.*, 7 (10), 11411–11422.
[10] Chen, X., Dong, Q., Chen, S., Zhang, Z., Zhang, X., Di, Y., Jiang, A., Zhang, D., and Li, T., 2023, Halloysite nanotubes supported $BiVO_4$/$BaSnO_3$ p-n heterojunction photocatalysts for the enhanced degradation of methylene blue under visible light, *Colloids Surf., A*, 664, 131143.
[11] Kamble, G.S., and Ling, Y.C., 2020, Solvothermal synthesis of facet-dependent $BiVO_4$ photocatalyst with enhanced visible-light-driven photocatalytic degradation of organic pollutant: Assessment of toxicity by zebrafish embryo, *Sci. Rep.*, 10 (1), 12993.
[12] Pham, M.Q., Ngo, T.M., Nguyen, V.H., Nong, L.X., Vo, D.V.N., Tran, T.V., Nguyen, T.D., Bui, X.T., and Nguyen, T.D., 2020, Facile solvothermal synthesis of highly active monoclinic scheelite $BiVO_4$ for photocatalytic degradation of methylene blue under white LED light irradiation, *Arabian J. Chem.*, 13 (11), 8388–8394.
[13] Phanichphant, S., Nakaruk, A., Chansaenpak, K., and Channei, D., 2019, Evaluating the photocatalytic efficiency of the $BiVO_4$/rGO photocatalyst, *Sci. Rep.*, 9 (1), 16091.
[14] Regmi, C., Kshetri, Y.K., Ray, S.K., Pandey, R.P., and Lee, S.W., 2017, Utilization of visible to NIR light energy by Yb^{+3}, Er^{+3} and Tm^{+3} doped $BiVO_4$ for the photocatalytic degradation of methylene blue, *Appl. Surf. Sci.*, 392, 61–70.
[15] Zhang, W., Wang, M., Zhao, W., and Wang, B., 2013, Magnetic composite photocatalyst $ZnFe_2O_4$/ $BiVO_4$: Synthesis, characterization, and visible-light photocatalytic activity, *Dalton Trans.*, 42 (43), 15464–15474.
[16] Kumar, M., Vaish, R., Sung, T.H., Kumar, A., and Yousef, E.S., 2023, Mechanochemical synthesis of $Bi_2VO_{5.5}$ for improved photocatalytic dye degradation, *Global Challenges*, 7 (4), 2200172.
[17] Jayavelu, Y., Maharana, G., Rajender, G., Muniramaiah, R., Divyadharshini, S., Baby, B.H., Kovendhan, M., Fernandes, J.M., and Joseph, D.P., 2024, Defect-mediated time-efficient photocatalytic degradation of methylene blue and ciprofloxacin using tungsten-incorporated ternary perovskite $BaSnO_3$ nanoparticles, *Chemosphere*, 351, 141128.
[18] Rungsawang, T., Krobthong, S., Paengpan, K., Kaewtrakulchai, N., Manatura, K., Eiad-Ua, A., Boonruang, C., and Wongrerkdee, S., 2024, Synergy of functionalized activated carbon and ZnO nanoparticles for enhancing photocatalytic degradation of methylene blue and carbaryl, *Radiat. Phys. Chem.*, 223, 111924.